Impact of fundamental molecular kinetics on macroscopic properties of high-enthalpy flows: The case of hypersonic atmospheric entry

G. Colonna,[1] F. Bonelli,[2,*] and G. Pascazio[2]
[1]*PLASMI Laboratory at CNR-NANOTEC, Bari, Italy*
[2]*Dipartimento di Meccanica Matematica e Management and Centro di Eccellenza in Meccanica Computazionale, Politecnico di Bari, via Re David 200, 70125, Bari, Italy*

(Received 20 June 2018; published 29 March 2019)

Thermochemical nonequilibrium is one of the most challenging issues when dealing with hypersonic flows experienced by objects (space vehicles, meteoroids, space debris) at atmospheric entry. The case of a hypersonic flow past a sphere is considered as a test model for systems in strong chemical and thermal nonequilibrium conditions, mimicking the extreme environment experienced by objects entering a planetary atmosphere. The problem has been studied using the state-to-state approach, calculating directly the distribution of vibrational levels of O_2 and N_2, together with the flow field, including also viscous effects. Nonequilibrium distributions are observed and the results have been compared with macroscopic experimental data, showing that the state-to-state model is able to provide better capabilities for predicting experimental results than the traditional multitemperature approach. The use of graphics processing units allowed us to obtain these results in a two-dimensional configuration, opening additional perspectives in the investigation of reacting flows.

DOI: 10.1103/PhysRevFluids.4.033404

I. INTRODUCTION

Thermochemical nonequilibrium at the molecular level may be reflected in global properties of macroscopic systems [1,2]. Nonequilibrium arises when relaxation time to thermal equilibrium is comparable or larger than the characteristic time in which the thermodynamic conditions of a system changes [3,4].

Such a fundamental phenomenon occurs in many fascinating physical problems and applications that stimulate human curiosity and research, e.g., interstellar gas clouds [5], the divertor in nuclear fusion reactors [6], discharges [7], laser-heated metals [8], rarefied gas dynamics [9] and high-enthalpy flows associated with hypersonic vehicles [10], hypersonic wind tunnels [11,12], and objects (space capsules [13–16], debris [17], and meteoroids [18]) entering a planetary atmosphere.

The latter problem presents two specific aspects. On one hand, it has been a critical outstanding problem since the beginning of the space race, when engineers and physicists had to face the re-entry into the atmosphere of a space capsule, and it is still one of the most important issues for space exploration. Indeed, predicting the flow properties around a space vehicle is vital to prevent its destruction [19–23]. On the other hand, it is a severe test model for systems in strong thermochemical nonequilibrium.

Concerning such a problem, classical gas dynamics models, based on the assumption either of an ideal gas or a reacting gas in thermochemical equilibrium, immediately were shown to be unsuitable for its description [3,24,25]. Indeed, a proper modeling of such phenomena requires a

*Corresponding author: francesco.bonelli@poliba.it

precise picture of the intimate nature of molecules with their different modes of storing energies (translational, rotational, vibrational, and electronic) and their quantum behavior allowing only discrete energy jumps [4,25–27]. Nevertheless, because of computational limitations, such accurate models could be used only for basic systems [28] and, for the purpose of defining an affordable design procedure, simplified multitemperature models [4,29] were developed that, when properly tuned using semiempirical parameters, showed acceptable results [30–33].

Nowadays, thanks to huge improvements in the field of high-performance computing (HPC) [34], detailed models, such as the state-to-state (StS) one [35–41], can be applied also to realistic two- and three-dimensional (2D-3D) geometries.

StS models are derived from fundamental chemical-physical theories [42] and, unlike multi-temperature models, assigning an independent temperature to each internal degree of freedom, they consider each internal level separately in order to be capable of determining its distribution even when it deviates from the equilibrium one. Consequently, for a neutral air mixture, the StS model involves more than 100 chemical species and about 10 000 reactions, compared with the 5 species, 3 temperatures, and 17 reactions of the multitemperature approach, thus explaining the higher computational cost.

In recent years, several research groups in the USA [38,43], Russia [44], and Europe [45], under the Phys4Entry project, have been investigating the StS model for hypersonic flows, devoting some efforts also to updating and completing state-selective rates [46]. A complete StS kinetic scheme is now available for the Earth (N_2/O_2) [35] and Jupiter atmospheres (H_2/He) [47,48], allowing calculations in a wide range of conditions.

In this work, theoretical (StS rates) and computational (HPC) developments are used in conjunction with the well-established Navier-Stokes equations within a GP-GPU (General-Purpose Computing on Graphics Processing Units) framework [49–51] in order to perform realistic 2D fluid dynamic simulations using the fundamental StS model [35,36]. The StS rates for atom-molecule collisions were obtained by QCT calculations on accurate PES (see Refs. [52–54]), while molecule-molecule collisions have been taken by extrapolating to high temperature the semiclassical calculation by Billing [55,56]. To the authors' knowledge, in the literature there are two multidimensional StS computations [57,58] coupled with the Navier-Stokes equations, but these works deal with N_2-N mixture, which is much less computationally demanding than the simulation of a more realistic air mixture. In these terms, we can surely state that this is one of the first 2D Navier-Stokes computations that include a StS kinetics for a neutral air mixture. It is anticipated that such a detailed model is essential to capture the physical phenomena correctly and to evaluate accurately macroscopic flow quantities required for the design process.

The case of a hypersonic flow past a sphere is considered as a test model for systems in strong chemical and thermal nonequilibrium conditions, mimicking the extreme environment experienced by an object entering the Earth atmosphere. In this problem, a strong shock wave drastically increases the gas temperature (up to 10 000 K), causing molecular excitation, dissociation, and ionization [25].

Thanks to data provided by the StS model, physical insights are given. The proposed model, showing distributions of internal states of the molecules, allowed us to solve a critical outstanding problem for realistic configurations, substantially advancing the field of aerothermodynamics and all those fields where thermochemical nonequilibrium phenomena are relevant [5–8,59,60]. The results here presented will show nonequilibrium distributions in contrast with the hypotheses on which the classical thermochemical nonequilibrium models are based. These physical insights will certainly be a stimulus for opening additional research with the aim to develop reduced models [61–63] consistent with physics.

The work is organized as follow: Section II presents the reactive Navier-Stokes equations, generalized for both the StS and Park models, and the numerical method; Sec. III shows the results obtained using the proposed numerical approach along with their comparison with experimental data and the results of the classical multitemperature approach; and finally, Sec. IV provides some concluding remarks.

II. GOVERNING EQUATIONS AND NUMERICAL METHOD

The physics of an atmospheric entry in the continuum regime has been investigated by solving the multicomponent reactive Navier-Stokes equations, that in integral form read

$$\int_{V_0} \frac{\partial}{\partial t}\mathbf{U}dV + \oint_{S_0} \mathbf{F}\cdot\mathbf{n}dS = \int_{V_0} \mathbf{W}dV, \tag{1}$$

where $\mathbf{U}$, $\mathbf{F}$ and $\mathbf{W}$ are the vectors of conservative variables, fluxes, and source term, respectively:

$$\mathbf{U} = [\rho_{1,1}, \ldots, \rho_{1,V_1}, \ldots, \rho_{S,1}, \ldots, \rho_{S,V_S}, \rho u, \rho v, \rho e, \rho_1\varepsilon_{vib,1}, \ldots, \rho_M\varepsilon_{vib,M}]^T, \tag{2}$$

$$\mathbf{F} = (\mathbf{F}_E - \mathbf{F}_V, \mathbf{G}_E - \mathbf{G}_V), \tag{3}$$

$$\begin{aligned}\mathbf{F}_E = [&\rho_{1,1}u, \ldots, \rho_{1,V_1}u, \ldots, \rho_{S,1}u, \ldots, \rho_{S,V_S}u, \rho u^2\\ &+ p, \rho uv, (\rho e + p)u, \rho_1\varepsilon_{vib,1}u, \ldots, \rho_M\varepsilon_{vib,M}u]^T,\end{aligned} \tag{4}$$

$$\begin{aligned}\mathbf{G}_E = [&\rho_{1,1}v, \ldots, \rho_{1,V_1}v, \ldots, \rho_{S,1}v, \ldots, \rho_{S,V_S}v, \rho uv, \rho v^2\\ &+ p, (\rho e + p)v, \rho_1\varepsilon_{vib,1}v, \ldots, \rho_M\varepsilon_{vib,M}v]^T,\end{aligned} \tag{5}$$

$$\begin{aligned}(\mathbf{F}_V, \mathbf{G}_V) = [&-\rho_{1,1}\mathbf{u}_{1,1}, \ldots, -\rho_{1,V_1}\mathbf{u}_{1,V_1}, \ldots, -\rho_{S,1}\mathbf{u}_{S,1}, \ldots, -\rho_{S,V_S}\mathbf{u}_{S,V_S}, \boldsymbol{\sigma}, \mathbf{u}\cdot\boldsymbol{\sigma} - \mathbf{q},\\ &-\mathbf{q}_1, \ldots, -\mathbf{q}_M]^T,\end{aligned} \tag{6}$$

$$\mathbf{W} = [\dot{\omega}_{1,1}, \ldots, \dot{\omega}_{1,V_1}, \ldots, \dot{\omega}_{S,1}, \ldots, \dot{\omega}_{S,V_S}, 0, 0, 0, \dot{\omega}_{vib,1}, \ldots, \dot{\omega}_{vib,M}]^T. \tag{7}$$

Here the density of the sth species in the lth internal state is given by $\rho_{s,l}$ (no state is considered in multitemperature models, i.e., $V_s = 1$), the thermodynamic pressure and the flow velocity components in the x and y directions are given by p, u, and v, respectively, e and $\varepsilon_{vib,m}$ represent the total energy per unit mass and the vibrational energy per unit mass of molecule m (the latter defined only for multitemperature models), respectively, S is the total number of species, and M is the total number of molecules. $\rho_s = \sum_l \rho_{s,l}$ and $\rho = \sum_s \rho_s$ provide the density of the sth component and the fluid density, respectively. The chemical and vibrational source terms are given by $\{\dot{\omega}_{s,l}\}$ and $\{\dot{\omega}_{vib,m}\}$ (the latter defined only for multitemperature models), respectively.

Diffusion velocity of the sth species in the lth internal state, viscous stress tensor, total energy heat flux, and vibrational energies heat flux ($\mathbf{q}_m$, $m = 1, \ldots, M$, defined only for multitemperature models) are modeled as follows:

$$\rho_{s,l}\mathbf{u}_{s,l} = -\rho D_s \nabla Y_{s,l}, \tag{8}$$

$$\boldsymbol{\sigma} = \mu[\nabla\mathbf{u} + (\nabla\mathbf{u})^T] - \frac{2}{3}\mu(\nabla\cdot\mathbf{u})\mathbf{I}, \tag{9}$$

$$\mathbf{q} = -\lambda_t\nabla T - \sum_{m=1}^{M}\lambda_{vib,m}\nabla T_{v,m} + \sum_{s=1}^{S}\sum_{l=1}^{V_s} h_{s,l}\rho_{s,l}\mathbf{u}_{s,l}, \tag{10}$$

$$\mathbf{q}_m = -\lambda_{vib,m}\nabla T_{v,m} + \varepsilon_{vib,m}\rho_m\mathbf{u}_m, \tag{11}$$

where Y is the mass fraction, T is the translational temperature, $T_{v,m}$ (defined only for the multitemperature models) is the vibrational temperature of molecule m, and $h_{s,l}$ is the specific enthalpy including translational-rotational, vibrational, and formation contributions, whereas transport coefficients, i.e., the mixture component diffusion coefficient, the mixture viscosity, the mixture translational conductivity, and the vibrational conductivity of molecule m are given by D_s, μ, λ_t, and $\lambda_{vib,m}$, respectively. Gupta's curve fits [64] were employed to evaluate single-component diffusion and viscosity coefficients, whereas the Eucken formula was used for the single-component

TABLE I. Test cases conditions.

Case	ρR [kg/m^2]	R [mm]	u_∞ [m/s]	Experimental normalized stand-off distance	Experimental error ±%
1	4×10^{-4}	7	3490	0.1129	1.33
2	4×10^{-4}	7	3370	0.1163	1.63
3	2×10^{-4}	7	3640	0.1137	2.99
4	2×10^{-4}	7	3360	0.1285	2.53
5	1×10^{-4}	15	2930	0.1372	1.10

translational and vibrational conductivities. Mixture properties were computed by using classical mixing rules [65–67], i.e., the Wilke rule and the Mason and Saxena adaptation for viscosity and conductivity, respectively, and a weighted harmonic mean for diffusion coefficients.

In order to close the system of governing equations, the perfect gas [68] assumption is employed to link p and e.

Both StS and multitemperature kinetic models have been implemented for the five-species air mixture (N_2, O_2, NO, N, O). The StS approach considers 68 and 47 levels for the N_2 and the O_2 molecules, respectively, and only the ground state ($l = 1$) is considered for the NO molecule and atomic species (N,O) [35,52,61,69,70], whereas for the multitemperature approach the Park model was used [4]. More details of the thermochemical models are provided in Appendices A and B.

The system of governing equations is solved numerically by using a finite-volume approach on a multiblock structured curvilinear mesh in an axial symmetric configuration [71]. The Steger and Warming [72] scheme, with the monotone upstream-centered schemes for conservation laws (MUSCL) reconstruction to get second-order accuracy, was used to solve inviscid fluxes, whereas we applied the Gauss divergence theorem and a linear reconstruction to compute viscous fluxes with second-order accuracy [71]. Finally, an explicit Runge-Kutta scheme is employed for time integration in conjunction with an operator splitting scheme to decouple fluid dynamics from stiff chemical source terms that were handled by using an implicit Gauss-Seidel algorithm [73]. More details can be found in Refs. [50,51].

III. RESULTS

The physical cases considered were the experimental test cases of Nonaka *et al.* [74]. Such experiments investigated the flow past a sphere in the intermediate hypersonic regime by firing samples in uncontaminated dry air and considering several sphere radii ($R = 7$, 14, and 15 mm) at different flight speeds (u_∞ between 2.44 and 3.85 km/s) and ambient pressures (p_∞ between 5.6×10^2 and 2.0×10^4 Pa).

We compare the results obtained by using both the Park and the StS models in reproducing the experimental measurements of Nonaka *et al.* [74]. Five test cases were considered, whose conditions are summarized in Table I [[74], Table 1]. All cases have the following free-stream and boundary conditions: $Y_{N_2} = 0.767$, $Y_{O_2} = 0.233$, $T_\infty = 293$ K [74,75], and, following Ref. [75], $T_{\text{wall}} = 1000$ K.

Previous investigations of viscous flow by Furudate *et al.* [75] have shown that in the intermediate hypersonic regime the Park model underestimates the shock stand-off distance.

Simulations were performed by using a computational grid (named the BASE grid) which includes 152×392 fluid cells. The grid is stretched in order to have a finer resolution both near the wall and the curved shock region. In order to show the validity of the results, a grid independence analysis and further proofs are provided in Appendix C.

As regards case 1, the Mach number contour plots obtained by using both the StS and the Park models are shown in Figs. 1(a) and 1(b), respectively, along with the experimental shock location. StS results are in better agreement with experiments compared to the Park model. This feature is

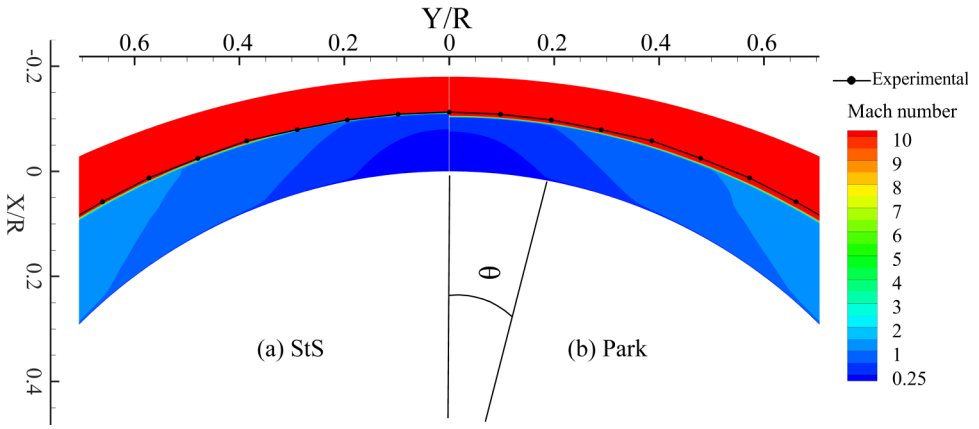

FIG. 1. Case 1: Numerical and experimental [[74], Fig. 10] shock shape (supposing that the experimental error is equal to that provided for the results along the stagnation line, see Table I, the bow shock error bar would fall inside the symbol dimension): (a) StS model and (b) Park model.

emphasized quantitatively in Fig. 2(a), showing the Mach number profiles along the stagnation line: The results of the Park and the StS models are provided along with the experimental shock location. The stand-off distance is well predicted by the StS model, whereas, as already shown by Furudate *et al.* [75], it is underestimated by the Park model. This behavior is the consequence of the higher density provided by the Park model [see Fig. 2(b)]. Indeed, as the density inside the shock layer is larger, the stand-off distance becomes shorter [76,77]. The density profiles also show the thermal boundary layer where density suddenly increases.

For the sake of truth, the StS model loses its advantages as dissociation decreases. Indeed, as shown in Figs. 3 and 2(a), the StS model provides results that are markedly more accurate than the one given by the Park model for cases 1, 2, and 3, whereas no appreciable improvements are shown for cases 4 and 5; in particular, in this latter case the Park model provides even better results. This behavior is due to the fact that dissociation in cases 4 and 5 is smaller (specifically, almost no

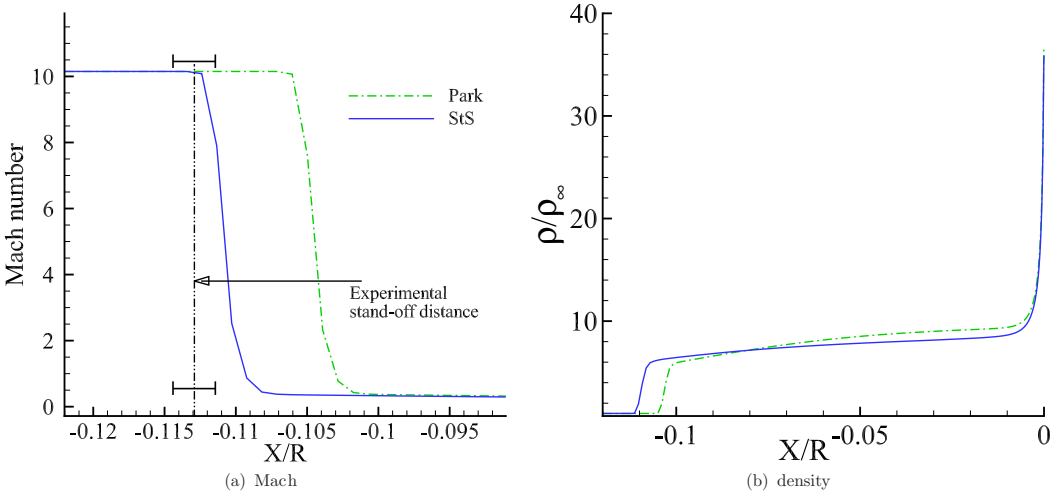

FIG. 2. Case 1: Stagnation line profiles: (a) closeup of the Mach number profiles at the shock position along with the experimental stand-off distance ($X/R = -0.1129 \pm 1.33\%$) [[74], row 18, Table 1] and (b) density profiles.

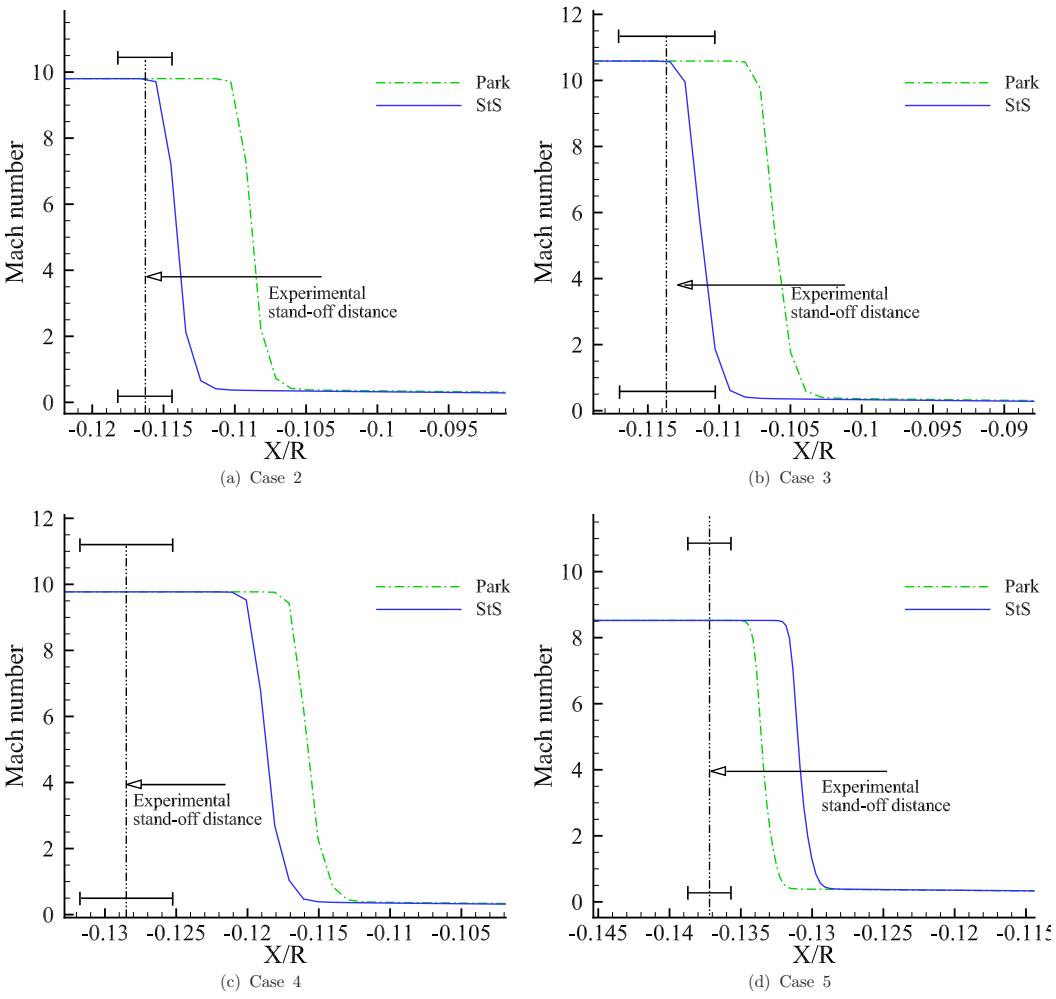

FIG. 3. Closeup of the Mach number stagnation line profiles at the shock position along with the experimental stand-off distance [[74], Table 1]: (a) case 2; (b) case 3; (c) case 4; and (d) case 5.

dissociation occurs in case 5), and therefore nonequilibrium effects are mainly thermal and the StS results are affected by the large uncertainties in the vibrational-translational by molecules (VTm) and vibrational-vibrational (VV) rates. This behavior has been already observed in Refs. [50,57], where it is shown that the Park model provides better predictions of vibrational relaxation in the case of $N_2 + N_2$ encounters.

In what follows, only the detailed results regarding case 1, which is representative of all cases that include both thermal and chemical nonequilibrium, will be presented and discussed.

Figure 4(a) shows that thermochemical nonequilibrium causes a reduction of the translational temperature after the peak reached downstream of the bow shock, due to vibrational excitation and chemical reactions that absorb energy at the expense of the translational degrees of freedom. Both thermochemical nonequilibrium models show similar vibrational temperature profiles with relevant differences. For both models, $T_v^{O_2}$ relaxes much faster than the nitrogen one, a behavior already observed by Furudate *et al.* [75], leading to the conjecture that the mismatch of the Park model with experiments was due to the assumption of equal vibrational temperatures. However, in order to verify such a conjecture, Furudate *et al.* [75] performed pure oxygen and pure nitrogen

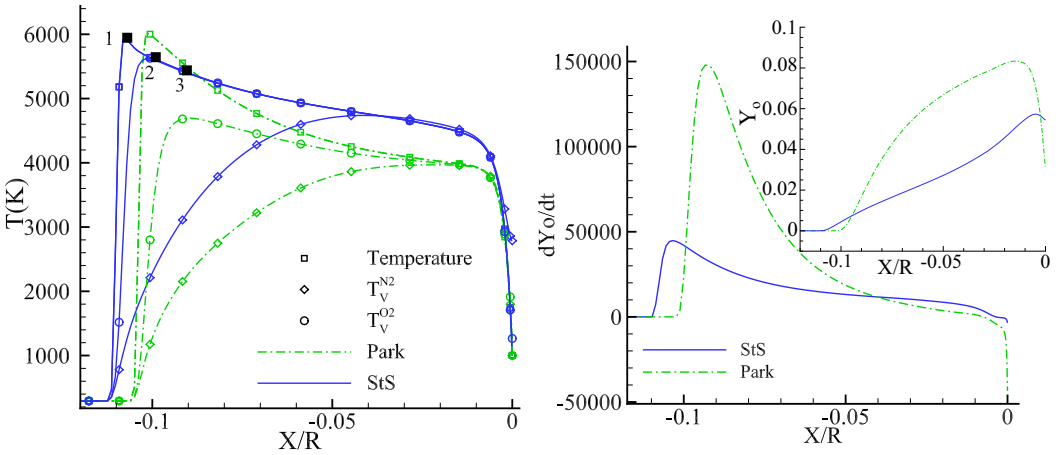

(a) temperature profiles

(b) oxygen atom reaction rate

FIG. 4. Case 1: Stagnation line profiles: (a) translational and vibrational temperature profiles. Points 1, 2, and 3 show the location along the stagnation line where vibrational distributions have been evaluated (see Fig. 5); (b) oxygen atom reaction rate: the inset shows the mass fractions of O (Y_O).

computations, instead of using air, and their hypothesis remained unproven. With the present results, we untangle this question, evidencing that the reason of the mismatch is due to chemical processes, and in particular to molecular dissociation.

Analyzing the stagnation line profile of atomic oxygen production source term [dY_O/dt; see Fig. 4(b)] due to dissociation ($O_2 + X \rightarrow 2O + X$), where X can be N_2, O_2, N, or O, it is evident that the Park model provides a much higher peak value and a larger reduction in translational temperature downstream of the bow shock, thus explaining the smaller stand-off distance. The footprint of the different reaction rates is given in the inset of Fig. 4(b), reporting the mass fractions of O (Y_O) along the stagnation line: The Park model gives larger O_2 dissociation.

The Park model predicts higher dissociation rates than StS, because it assumes Boltzmann vibrational distributions and relates the rate coefficients to the effective temperature $T_{\text{eff}} = T_v^{\gamma} T^{1-\gamma}$, an assumption contradicted by the StS model [69]. In order to better understand the nonequilibrium phenomena involved downstream of a compression wave, the vibrational distributions calculated with the StS approach and the theoretical Boltzmann ones (evaluated by considering the vibrational temperature of the first two levels [[51], Eq. 29]), for both N_2 and O_2 molecules, are given in Fig. 5. Three probes (indicated with numbers 1, 2, and 3), located along the stagnation streamline and downstream of the shock wave, were considered [see Fig. 4(a)]. The insets of Fig. 5 provide also the ratio between the actual distributions and the Boltzmann ones in order to give a more quantitative view. Just downstream of the bow shock, the vibrational distribution of N_2 clearly departs from the Boltzmann one. Distribution tails show a significant overpopulation [see the inset of Fig. 5(a)] due to vibrational excitation. The distributions can be divided in three energy regions, each one described by a Boltzmann distribution with a different vibrational temperature [62]. The high-energy distribution is determined by the balance between VT and dissociation and the low-energy part mainly by VT, while the distribution at intermediate vibrational quantum numbers is a transition region, mainly determined by multiquantum VT by atomic collisions. On the other hand, O_2 vibrational distributions [Fig. 5(b)] show an overpopulation just downstream of the bow shock (except for the higher vibrational levels) due to vibrational excitation, but further downstream O_2 dissociation causes an important underpopulation, with the exception of low-lying levels well approximated by a Boltzmann distribution.

The same analysis was performed by considering four probes at the wall surface and the results are shown in Fig. 6. It should be noted that at the wall the translational temperature is fixed at 1000 K

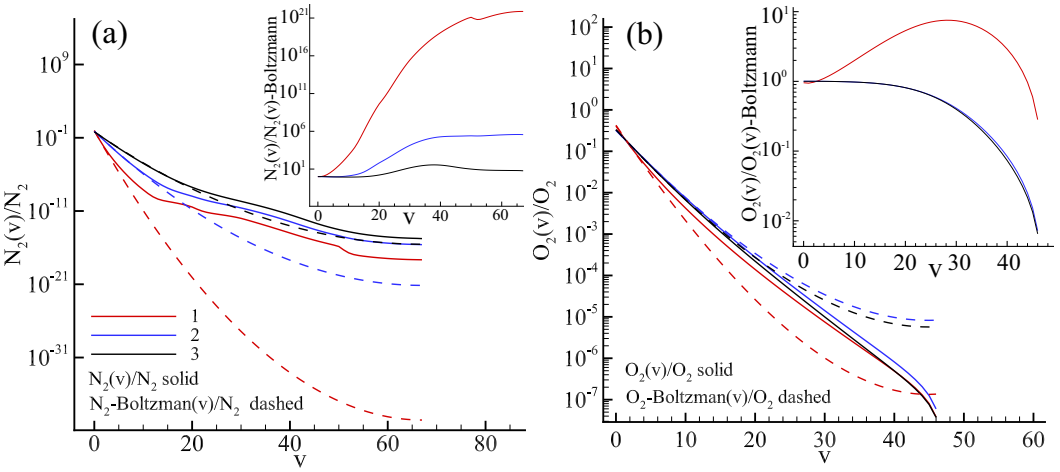

FIG. 5. Case 1: stagnation line populations with actual to Boltzmann ratio in the inset: (a) N_2 and (b) O_2. Populations have been evaluated along the stagnation streamline and downstream of the shock wave at probes 1, 2, and 3 whose locations are given in Fig. 4(a).

with a noncatalytic surface. Again, N_2 and O_2 are far from internal equilibrium. Contrary to what is seen just downstream of the bow shock, N_2 shows a significant underpopulation of the highly excited levels, while O_2 shows a huge overpopulation of the higher levels due to the partial recombination occurring in the thermal boundary layer, preferentially populating high-energy levels.

The nonequilibrium character of the distributions is generalized in the flow field, as can be observed in Fig. 7, which reports the contour plot of the ratio of the actual distribution and the extrapolated Boltzmann for the last vibrational level of N_2 and O_2.

The differences in the results obtained by using the StS and the Park models rely on the non-Boltzmann behaviors of the vibrational distribution [78,79]. The distribution tail is not correlated with the vibrational temperature, which represents the low-energy distribution. As a consequence, the global dissociation rates predicted by the multitemperature approach can be under- or overestimated depending on the deviations of the distribution from a Boltzmann one.

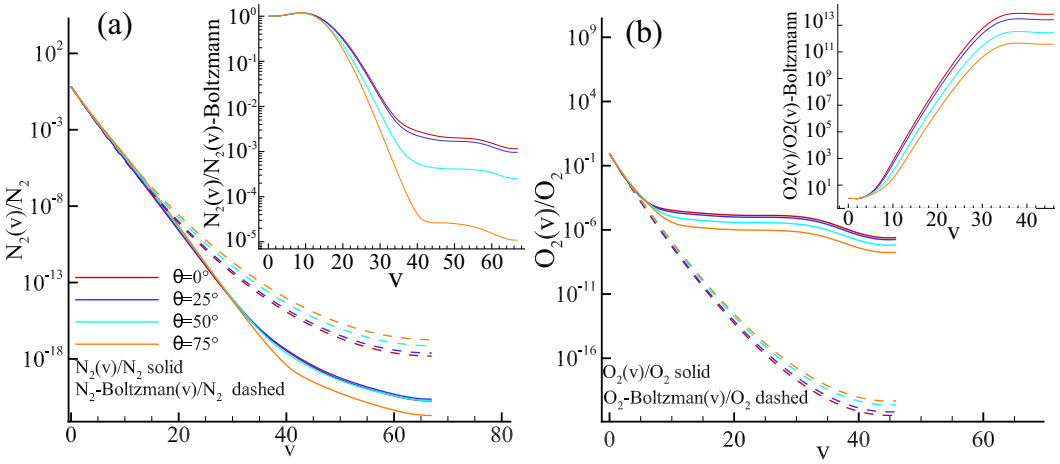

FIG. 6. Case 1: wall surface populations with the actual to Boltzmann ratio in the inset: (a) N_2 and (b) O_2. The azimuthal angle θ is defined in Fig. 1.

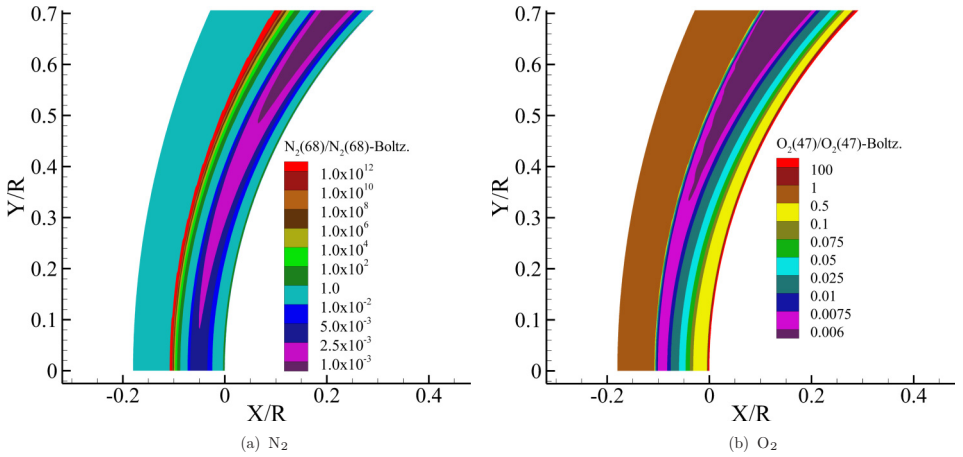

(a) N_2 (b) O_2

FIG. 7. Case 1: actual to Boltzmann ratio for the highest vibrational level: (a) N_2 and (b) O_2.

IV. CONCLUSIONS

The results here reported have shown that a detailed description of the molecular structure is needed to predict macroscopic behaviors of high-enthalpy flows. Specifically, the StS model provides a stand-off distance that is in a better agreement with experiments when both thermal and chemical nonequilibrium are not negligible. This behavior is due to non-Boltzmann distributions of vibrational levels that strongly affect reaction rates.

The present numerical approach shows the feasibility of StS modeling also in real systems renewing the field of aerothermodynamics. Such approach provides additional insights, allowing us to better understand the physics behind the scenes and the limits of classical macroscopic models in reproducing experimental results and opening additional perspectives for building more accurate reduced models.

ACKNOWLEDGMENTS

The authors gratefully acknowledge Michele Tuttafesta and Luigi Cutrone for their help in developing the code and for fruitful discussion.

APPENDIX A: STS MODEL

For a five-species neutral air mixture, the vibrationally resolved StS model employed in this work considers 68 and 47 vibrational levels for the N_2 and O_2 molecules, respectively, whereas for the N, O, and NO species only the ground state was taken into account. The formation energies in electron volts, referred to N_2 and O_2 molecules, are 0.941, 2.55764, and 4.88195 for NO, O, and N respectively. A transport equation is written for each vibrational level, where source terms are computed according to vibrational-translational (VT) and vibrational-vibrational (VV) energy exchanges and dissociation recombination (DR) or ladder climbing (LD) processes due to collisions with atoms (a) and molecules (m) [35]. VV and VT by molecules (VTm) only consider monoquantum transitions, and rate coefficients have been calculated using semiclassical approach [80–82]. The rates have been fitted using the Schwartz, Slawsky, and Herzfeld (SSH) expression, except for N_2-N_2 VTm, whose expression is reported in Ref. [61]. Nevertheless, these rates have been calculated considering 46 vibrational levels for N_2 and 32 for O_2. In this paper, the rates have been scaled to the present level scheme. The atom-molecule processes have been calculated by QCT and include multiquantum transitions [37,70]. Dissociation resulting

by molecule-molecule collisions have the same dependence on the vibrational quantum number as atom-molecule dissociation, normalized in such a way that the thermal rate reproduces the experimental one [61]. The full list of processes is as follows (where v and w are generic vibrational levels or vibrational quantum numbers):

$$N_2(v) + N_2(w) \leftrightarrow N_2(v-1) + N_2(w+1) \quad \text{(VV)}, \tag{A1}$$

$$N_2(v) + N_2 \leftrightarrow N_2(v-1) + N_2 \quad \text{(VTm)}, \tag{A2}$$

$$N_2(v) + N \leftrightarrow N_2(v-\Delta v) + N \quad \text{(VTa)}, \tag{A3}$$

$$O_2(v) + O_2(w) \leftrightarrow O_2(v-1) + O_2(w+1) \quad \text{(VV)}, \tag{A4}$$

$$O_2(v) + O_2 \leftrightarrow O_2(v-1) + O_2 \quad \text{(VTm)}, \tag{A5}$$

$$O_2(v) + O \leftrightarrow O_2(v-\Delta v) + O \quad \text{(VTa)}, \tag{A6}$$

$$N_2(v) + O_2 \leftrightarrow N_2(v-1) + O_2 \quad \text{(VTm)}, \tag{A7}$$

$$N_2(v) + O \leftrightarrow N_2(v-1) + O \quad \text{(VTa)}, \tag{A8}$$

$$O_2(v) + N_2 \leftrightarrow O_2(v-1) + N_2 \quad \text{(VTm)}, \tag{A9}$$

$$O_2(v) + N \leftrightarrow O_2(v-1) + N \quad \text{(VTa)}, \tag{A10}$$

$$O_2(v) + N_2(w-1) \leftrightarrow O_2(v-2) + N_2(w) \quad \text{(VV)}, \tag{A11}$$

$$N_2(v) + N_2 \leftrightarrow 2N + N_2 \quad \text{(DRm)}, \tag{A12}$$

$$N_2(v) + N \leftrightarrow 2N + N \quad \text{(DRa)}, \tag{A13}$$

$$O_2(v) + O_2 \leftrightarrow 2O + O_2 \quad \text{(DRm)}, \tag{A14}$$

$$O_2(v) + O \leftrightarrow 2O + O \quad \text{(DRa)}, \tag{A15}$$

$$N_2(v_{max}) + O_2 \leftrightarrow N_2(v_{max}+1) + O_2 \equiv 2N + O_2 \quad \text{(LCm)}, \tag{A16}$$

$$N_2(v_{max}) + O \leftrightarrow N_2(v_{max}+1) + O \equiv 2N + O \quad \text{(LCa)}, \tag{A17}$$

$$O_2(v_{max}) + N_2 \leftrightarrow O_2(v_{max}+1) + N_2 \equiv 2O + N_2 \quad \text{(LCm)}, \tag{A18}$$

$$O_2(v_{max}) + N \leftrightarrow O_2(v_{max}+1) + N \equiv 2O + N \quad \text{(LCa)}. \tag{A19}$$

Also, NO dissociation processes were considered,

$$NO + X \leftrightarrow N + O + X, \tag{A20}$$

where X is a generic component, i.e., N, O, NO, O_2, or N_2, and Zeldovich [83,84] reactions are

$$O_2(v) + N \leftrightarrow NO + O, \tag{A21}$$

$$N_2(v) + O \leftrightarrow NO + N, \tag{A22}$$

for a total of about 10 000 elementary processes.

APPENDIX B: MULTITEMPERATURE PARK MODEL

For a five-species neutral air mixture, the Park model considers the following dissociation and Zeldovich (exchange) reactions:

$$N_2 + X \leftrightarrow 2N + X, \tag{B1}$$

$$O_2 + X \leftrightarrow 2O + X, \tag{B2}$$

$$NO + X \leftrightarrow N + O + X, \tag{B3}$$

$$NO + O \leftrightarrow N + O_2, \tag{B4}$$

$$N_2 + O \leftrightarrow NO + N, \tag{B5}$$

where X is the generic collision partner, i.e., N_2, O_2, NO, N, or O, for a total of 17 reactions.

Forward rate coefficients are evaluated by using the semiempirical Arrhenius law,

$$k_{f_i} = A_i T_{\text{eff}}^{n_i} \exp\left(-\frac{T_{d_i}}{T_{\text{eff}}}\right), \tag{B6}$$

where the subscript i indicates the generic reaction, whereas constants A_i, n_i, and T_{d_i} are given in Table II. In the case of dissociation reactions of molecule m, the effective temperature T_{eff_m} is a geometrically averaged temperature of the translational (T) and vibrational (T_{v_m}) temperature, i.e.,

$$T_{\text{eff}_m} = T_{v_m}^{\gamma} T^{1-\gamma}, \tag{B7}$$

where γ is a parameter here assumed equal to 0.5, whereas T_{eff} is the translational temperature (T) for the Zeldovich (exchange) reactions [[4], p. 138], [85].

TABLE II. Reaction rate coefficients from Refs. [[4], p. 326] and [85] ($\text{cm}^3\ \text{mol}^{-1}\ \text{s}^{-1}$).

Reaction	X	T_{eff}	A ($\text{cm}^3\ \text{mol}^{-1}\ \text{s}^{-1}$)	n	T_d (K)
$N_2 + X \leftrightarrow 2N + X$	N	$(TT_{v_{N_2}})^{0.5}$	3.0×10^{22}	−1.60	113200
	O		3.0×10^{22}		
	N_2		7.0×10^{21}		
	O_2		7.0×10^{21}		
	NO		7.0×10^{21}		
$O_2 + X \leftrightarrow 2O + X$	N	$(TT_{v_{O_2}})^{0.5}$	1.0×10^{22}	−1.50	59500
	O		1.0×10^{22}		
	N_2		2.0×10^{21}		
	O_2		2.0×10^{21}		
	NO		2.0×10^{21}		
$NO + X \leftrightarrow N + O + X$	N	$(TT_{v_{NO}})^{0.5}$	1.1×10^{17}	0.0	75500
	O		1.1×10^{17}		
	N_2		5.0×10^{15}		
	O_2		5.0×10^{15}		
	NO		1.1×10^{17}		
$NO + O \leftrightarrow N + O_2$		T	8.4×10^{12}	0.0	19400
$N_2 + O \leftrightarrow NO + N$		T	6.4×10^{17}	−1.0	38400

TABLE III. Equilibrium constant coefficients from Ref. [[4], p. 35].

Reaction	A_1	A_2	A_3	A_4	A_5
$N_2 + X \leftrightarrow 2N + X$ [mol/cm^3]	1.476600	1.629100	1.215300	−11.457000	−0.009444
$O_2 + X \leftrightarrow 2O + X$ [mol/cm^3]	0.509890	2.477300	1.713200	−6.544100	0.029591
$NO + X \leftrightarrow N + O + X$ [mol/cm^3]	0.507650	0.735750	0.480420	−7.497900	−0.016247
$NO + O \leftrightarrow N + O_2$	−0.002428	−1.741500	−1.233100	−0.953650	−0.045850
$N_2 + O \leftrightarrow NO + N$	0.969210	0.893290	0.735310	−3.959600	0.006818

Backward reaction rate coefficients are computed by using the equilibrium constant,

$$K_{eq_i} = \frac{k_{f_i}}{k_{b_i}}, \tag{B8}$$

evaluated by using the following expression [[4], p. 24],

$$K_{eq_i} = \exp[A_1(T_{\text{eff}}/10\,000) + A_2 + A_3 \ln(10\,000/T_{\text{eff}}) + A_4(10\,000/T_{\text{eff}}) + A_5(10\,000/T_{\text{eff}})^2], \tag{B9}$$

whose constants are given in Table III.

The sum of a collisional ($\dot{\omega}_{LT,m}$) and a chemical ($\dot{\omega}_{chem,m}$) [[4], p. 125] contribution is employed to express the vibrational energy source term of molecule m ($\dot{\omega}_{vib,m}$).

The Landau-Teller equation is used to evaluate the collisional term

$$\dot{\omega}_{LT,m} = \rho_m \frac{\varepsilon_{vib,m}(T) - \varepsilon_{vib,m}(T_{v_m})}{\tau_m}, \tag{B10}$$

where τ_m is the relaxation time, computed by using the Millikan-White formula [86], [[4], p. 58], [85] plus a high-temperature correction [[4], p. 60] [85] and $\varepsilon_{vib,m}(T)$ is the vibrational energy at equilibrium.

Regarding the chemical ($\dot{\omega}_{chem,m}$) contribution, the energy exchanged in the dissociation processes is equally divided between the translational and vibrational degrees of freedom. Therefore, indicating with D_m the dissociation energy per unit mass of molecule m, the following expression is employed [[4], pp. 107, 126],

$$\dot{\omega}_{chem,m} = \frac{D_m}{2}\dot{\omega}_m. \tag{B11}$$

Further details can be found in Refs. [33,51].

APPENDIX C: GRID INDEPENDENCE ANALYSIS

In order to show grid independence of the results, a computation with a finer grid, called FINE and obtained by halving the grid spacing of the BASE grid, was performed. To avoid an excessive computational cost, the analysis was performed by using only the Park model. Figure 8(a) shows the Mach number profiles obtained with the Park model for both the FINE and BASE grids. Even if the FINE grid provides a smaller shock thickness, the shock location is not affected by the grid resolution. Grid accuracy is further demonstrated in Fig. 8(b), showing the temperature profiles obtained with both the FINE and BASE grids: Profiles are coincident within plotting accuracy. Finally, another proof is given in Fig. 9 where the Mach number contour plot, computed with the BASE grid, and the Mach isolines, computed with the FINE grid, are given: The two grids provide

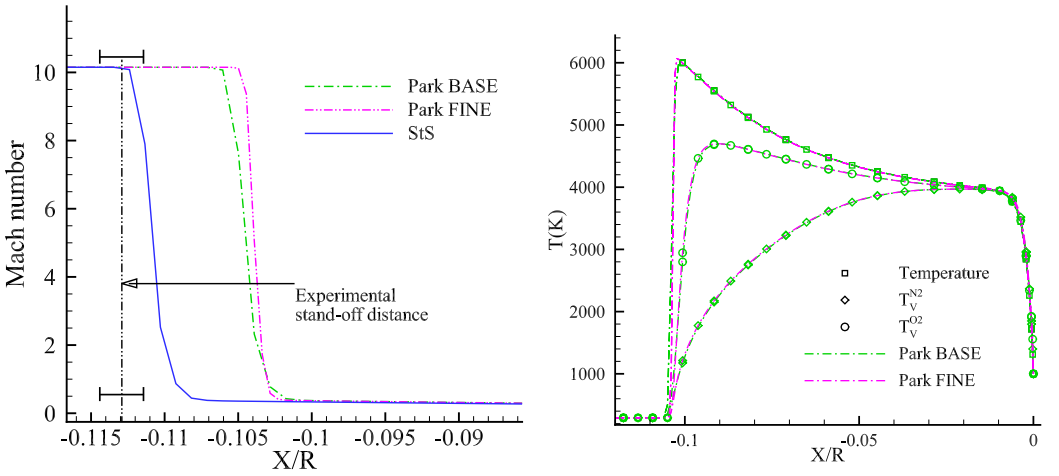

(a) Mach (b) Temperature

FIG. 8. Case 1: grid convergence study performed with the Park model: Mach number (a) and temperature profiles (b) along the stagnation line for both the BASE and FINE grid.

exactly the same results. Moreover, the time-step independence was also verified by comparing the results obtained by using CFL equal to 0.3 and 0.6 on the BASE grid. Finally, the convergence of the Gauss-Seidel algorithm, used to treat the chemical source terms, was verified by doubling the number of iterative steps.

APPENDIX D: DENSITY, TEMPERATURE, AND PRESSURE CONTOUR PLOTS

In order to better show the differences in terms of thermodynamic variables between the findings provided by the Park and the StS models, the contour plots of temperature, density, and pressure are given in Fig. 10 for case 1. The Park model provides lower temperature values in the shock layer and higher densities, thus explaining the lower predicted value of the stand-off distance.

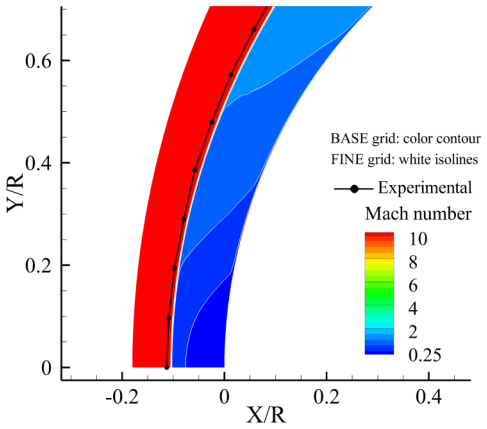

FIG. 9. Case 1: grid convergence study performed with the Park model: contour plot and isolines of the Mach number computed on the BASE and on the FINE grid, respectively. The bow-shock experimental position is also shown.

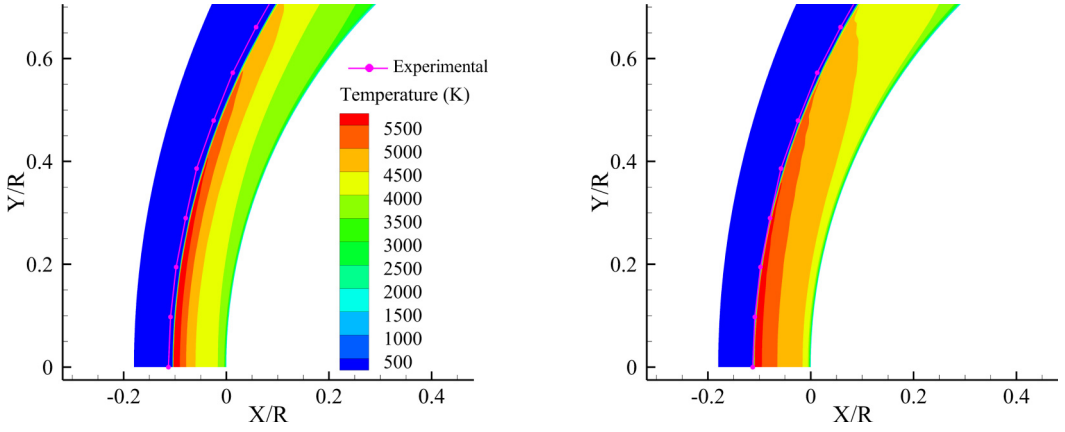

(a) temperature

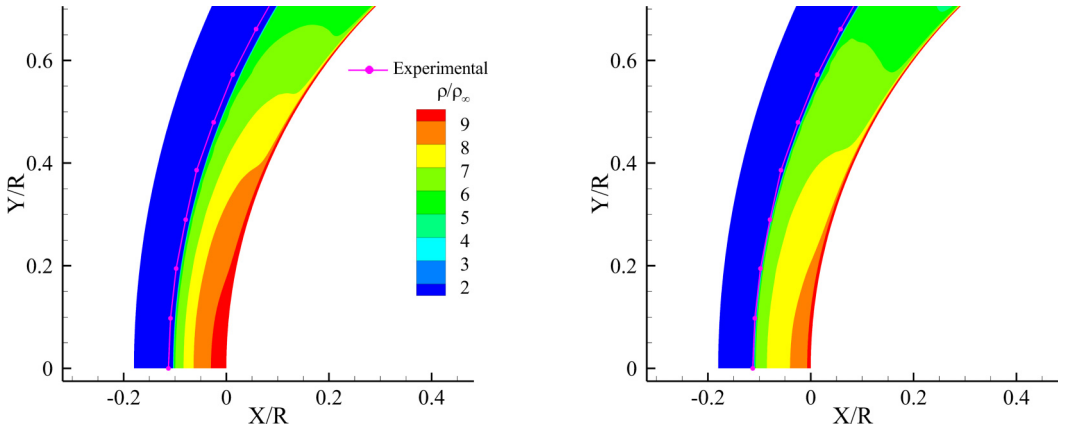

(b) density

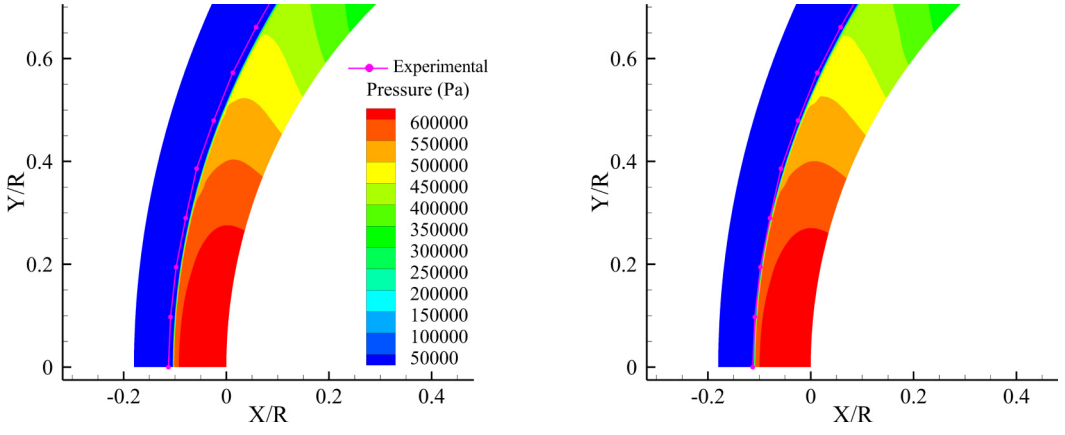

(c) pressure

FIG. 10. Case 1: (a) Temperature, (b) density, and (c) pressure contour plots: (left) Park and (right) StS.

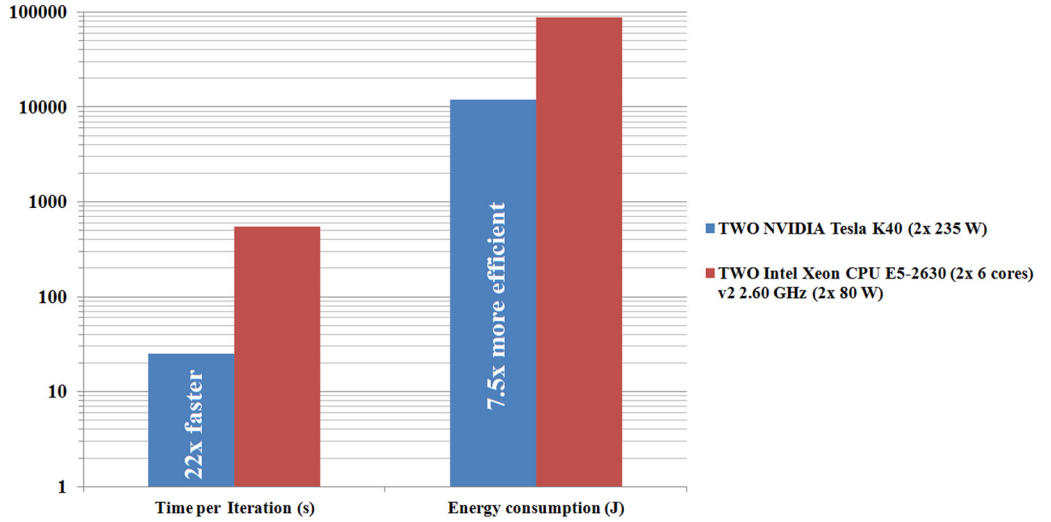

FIG. 11. Comparison between GPU and CPU performance in terms of time per iteration (s) and energy consumption per iteration (J) by considering the BASE grid (152 × 392 fluid cells) and the setup of case 1.

APPENDIX E: GPU PERFORMANCE

In this section, a comparison between GPU and CPU performance, in terms of computational time (time per iteration) and energy consumption needed to execute an iteration, is presented. The results here presented were obtained by considering the BASE grid (152 × 392 fluid cells) and the setup of case 1. The chemical equation was advanced in time by using 1 subtime step and 16 inner iterations for the Gauss-Seidel algorithm. Only the StS model was considered. Simulations were performed on one node of our GPU cluster hosting two NVIDIA Tesla K40m (235 W) and two Intel(R) Xeon(R) CPU E5-2630 v2 2.60 GHz (80 W) processors.

One iteration is performed in about 25 s when running on two Tesla K40 processors, with an energy consumption of 11.9 kJ, and in about 550 s when running on two Xeon E5-2630 processors, with an energy consumption of 88.3 kJ (see Fig. 11). Thus, for this test case, GPU is 22 times faster and about 7.5 times more efficient than CPU. Even better results can be obtained by increasing the number of fluid cells as shown in Ref. [51].

[1] D. Bruno, M. Capitelli, and S. Longo, DSMC modelling of vibrational and chemical kinetics for a reacting gas mixture, Chem. Phys. Lett. **289**, 141 (1998).

[2] D. Bruno, M. Capitelli, F. Esposito, S. Longo, and P. Minelli, Direct simulation of non-equilibrium kinetics under shock conditions in nitrogen, Chem. Phys. Lett. **360**, 31 (2002).

[3] W. G. Vincenti and C. H. Kruger, *Introduction to Physical Gas Dynamics* (Wiley, New York, 1965).

[4] C. Park, *Nonequilibrium Hypersonic Aerothermodynamics* (Wiley, New York, 1990).

[5] J. R. Goicoechea, J. Pety, S. Cuadrado, J. Cernicharo, E. Chapillon, A. Fuente, M. Gerin, C. Joblin, N. Marcelino, and P. Pilleri, Compression and ablation of the photo-irradiated molecular cloud the orion bar, Nature (London) **537**, 207 (2016).

[6] E. Pawelec, T. Dittmar, A. Drenik, A. Meigs, and JET contributors, Molecular ND band spectroscopy in the divertor region of nitrogen seeded jet discharges, J. Phys. Conf. Ser. **959**, 012009 (2018).

[7] M. Capitelli, G. Colonna, G. D'Ammando, V. Laporta, and A. Laricchiuta, The role of electron scattering with vibrationally excited nitrogen molecules on non-equilibrium plasma kinetics, Phys. Plasmas **20**, 101609 (2013).
[8] K.-i. Inoue, K. Watanabe, T. Sugimoto, Y. Matsumoto, and T. Yasuike, Disentangling Multidimensional Nonequilibrium Dynamics of Adsorbates: CO Desorption from Cu(100), Phys. Rev. Lett. **117**, 186101 (2016).
[9] R. R. Gazizulin, O. Maillet, X. Zhou, A. M. Cid, O. Bourgeois, and E. Collin, Surface-Induced Near-Field Scaling in the Knudsen Layer of a Rarefied Gas, Phys. Rev. Lett. **120**, 036802 (2018).
[10] F. Bonelli, L. Cutrone, R. Votta, A. Viggiano, and V. Magi, Preliminary design of a hypersonic air-breathing vehicle, in *17th AIAA International Space Planes and Hypersonic Systems and Technologies Conference, 11–14 April 2011, San Francisco, California, AIAA 2011-2319* (AIAA, Red Hook, NY, 2011).
[11] M. Auweter-Kurtz, H. L. Kurtz, and S. Laure, Plasma generators for re-entry simulation, J. Propul. Power **12**, 1053 (1996).
[12] C. Purpura, F. De Filippis, P. Barrera, and D. Mandanici, Experimental characterisation of the CIRA plasma wind tunnel Scirocco test section, Acta Astronautica **62**, 410 (2008).
[13] P. N. Desai, D. T. Lyons, J. Tooley, and J. Kangas, Entry, descent, and landing operations analysis for the stardust entry capsule, J. Spacecr. Rockets **45**, 1262 (2008).
[14] S. Surzhikov, High-enthalpy radiating flows in aerophysics, in *Plasma Modeling: Methods and Applications*, edited by G. Colonna and A. D'Angola, Plasma Physics Series (IOP, Bristol, UK, 2016), Chap. 12.
[15] D. R. Olynick, W. D. Henline, L. H. Chambers, and G. V. Candler, Comparison of coupled radiative flow solutions with project fire II flight data, J. Thermophys. Heat Transfer **9**, 586 (1995).
[16] F. Massobrio, R. Viotto, M. Serpico, A. Sansone, M. Caporicci, and J.-M. Muylaert, Expert: An atmospheric re-entry test-bed, Acta Astronautica **60**, 974 (2007).
[17] S. Tkatchova, Space debris mitigation, *Emerging Space Markets* (Springer, Berlin, 2018), pp. 93–105.
[18] A. P. Kartashova, O. P. Popova, D. O. Glazachev, P. Jenniskens, V. V. Emel'yanenko, E. D. Podobnaya, and A. Y. Skripnik, Study of injuries from the Chelyabinsk airburst event, Planet. Space Sci. **160**, 107 (2018).
[19] T. Reichhardt, NASA braced for culture shock as Columbia inquiry reaches verdict, Nature (London) **424**, 863 (2003).
[20] D. Butler, Shuttle inquiry to piece disaster together from the ground up, Nature (London) **421**, 677 (2003).
[21] C. Seife, NASA's hypersonic lab studies factors leading to breakup, Science **299**, 1971 (2003).
[22] J. J. Bertin and R. M. Cummings, Fifty years of hypersonics: Where we've been, where we're going, Progr. Aerospace Sci. **39**, 511 (2003).
[23] J. D. Schmisseur, Hypersonics into the 21st century: A perspective on AFOSR-sponsored research in aerothermodynamics, Progr. Aerospace Sci. **72**, 3 (2015).
[24] H. G. Hornung, Non-equilibrium dissociating nitrogen flow over spheres and circular cylinders, J. Fluid Mech. **53**, 149 (1972).
[25] J. D. Anderson, *Hypersonic and High-Temperature Gas Dynamics* (McGraw-Hill, New York, 1988).
[26] J. D. Teare, R. L. Taylor, and C. W. von Rosenberg, Observations of vibration-vibration energy pumping between diatomic molecules, Nature (London) **225**, 240 (1970).
[27] M. Panesi, T. E. Magin, A. Bourdon, A. Bultel, and O. Chazot, Electronic excitation of atoms and molecules for the fire II flight experiment, J. Thermophys. Heat Transfer **25**, 361 (2011).
[28] G. Colonna, M. Tuttafesta, and D. Giordano, Numerical methods to solve euler equations in one-dimensional steady nozzle flow, Comput. Phys. Commun. **138**, 213 (2001).
[29] C. Park, R. L. Jaffe, and H. Partridge, Chemical-kinetic parameters of hyperbolic earth entry, J. Thermophys. Heat Transfer **15**, 76 (2001).
[30] S. Surzhikov and J. Shang, Fire-II flight data simulations with different physical-chemical kinetics and radiation models, Front. Aerospace Eng. **4**, 70 (2015).
[31] J. Hao and C.-Y. Wen, Numerical investigation of oxygen thermochemical nonequilibrium on high-enthalpy double-cone flows, Int. J. Heat Mass Transf. **127**, Part B, 892 (2018).

[32] J. Hao and C.-Y. Wen, Effects of vibrational nonequilibrium on hypersonic shock-wave/laminar boundary-layer interactions, Int. Commun. Heat Mass Transfer **97**, 136 (2018).
[33] F. Bonelli, M. Tuttafesta, G. Colonna, L. Cutrone, and G. Pascazio, Numerical investigation of high enthalpy flows, Energy Proced. **126**, 99 (2017).
[34] S. Fiore, M. Bakhouya, and W. W. Smari, On the road to exascale: Advances in high performance computing and simulations—an overview and editorial, Future Generation Comp. Sys. **82**, 450 (2018).
[35] M. Capitelli, R. Celiberto, G. Colonna, F. Esposito, C. Gorse, K. Hassouni, A. Laricchiuta, and S. Longo, *Fundamental Aspects of Plasma Chemical Physics: Kinetics*, Springer Series on Atomic, Optical and Plasma Physics (Springer Science & Business Media, New York, 2016), Vol. 85.
[36] M. Capitelli, I. Armenise, D. Bruno, M. Cacciatore, R. Celiberto, G. Colonna, O. De Pascale, P. Diomede, F. Esposito, C. Gorse *et al.*, Non-equilibrium plasma kinetics: A state-to-state approach, Plasma Sources Sci. Technol. **16**, S30 (2007).
[37] F. Esposito and M. Capitelli, QCT calculations for the process $N_2(v) + N \rightarrow N_2(v') + N$ in the whole vibrational range, Chem. Phys. Lett. **418**, 581 (2006).
[38] R. Jaffe, D. Schwenke, G. Chaban, and W. Huo, Vibrational and rotational excitation and relaxation of nitrogen from accurate theoretical calculations, in *46th AIAA Aerospace Sciences Meeting and Exhibit* (AIAA, New York, 2008), p. 1208.
[39] J. D. Bender, P. Valentini, I. Nompelis, T. E. Schwartzentruber, and G. V. Candler, Characterization of vibrational and rotational energy transfer in N_2-N_2 dissociative collisions using the quasiclassical trajectory method, in *45th AIAA Thermophysics Conference* (AIAA, New York, 2015), p. 3253.
[40] R. S. Chaudhry, M. S. Grover, J. D. Bender, T. E. Schwartzentruber, and G. V. Candler, Quasiclassical trajectory analysis of oxygen dissociation via O_2, O, and N_2, in *2018 AIAA Aerospace Sciences Meeting* (AIAA, New York, 2018), p. 0237.
[41] J. Werdecker, M. E. van Reijzen, B.-J. Chen, and R. D. Beck, Vibrational Energy Redistribution in a Gas-Surface Encounter: State-To-State Scattering of CH_4 from Ni(111), Phys. Rev. Lett. **120**, 053402 (2018).
[42] F. Esposito, M. Capitelli, and C. Gorse, Quasi-classical dynamics and vibrational kinetics of $N + N_2$ (v) system, Chem. Phys. **257**, 193 (2000).
[43] D. Andrienko and I. D. Boyd, Investigation of oxygen vibrational relaxation by quasi-classical trajectory method, Chem. Phys. **459**, 1 (2015).
[44] E. V. Kustova and G. M. Kremer, Chemical reaction rates and non-equilibrium pressure of reacting gas mixtures in the state-to-state approach, Chem. Phys. **445**, 82 (2014).
[45] A. Munafo, M. Panesi, R. L. Jaffe, G. Colonna, A. Bourdon, and T. E. Magin, QCT-based vibrational collisional models applied to nonequilibrium nozzle flows, Eur. Phys. J. D **66**, 188 (2012).
[46] http://users.ba.cnr.it/imip/cscpal38/phys4entry/index.html.
[47] G. Colonna, L. D. Pietanza, and G. d'Ammando, Self-consistent collisional-radiative model for hydrogen atoms: Atom–atom interaction and radiation transport, Chem. Phys. **398**, 37 (2012).
[48] G. Colonna, G. D'Ammando, L. D. Pietanza, and M. Capitelli, Excited-state kinetics and radiation transport in low-temperature plasmas, Plasma Phys. Controlled Fusion **57**, 014009 (2014).
[49] M. Tuttafesta, G. Colonna, and G. Pascazio, Computing unsteady compressible flows using Roe's flux-difference splitting scheme on GPUs, Comput. Phys. Commun. **184**, 1497 (2013).
[50] M. Tuttafesta, G. Pascazio, and G. Colonna, Multi-GPU unsteady 2D flow simulation coupled with a state-to-state chemical kinetics, Comput. Phys. Commun. **207**, 243 (2016).
[51] F. Bonelli, M. Tuttafesta, G. Colonna, L. Cutrone, and G. Pascazio, An MPI-CUDA approach for hypersonic flows with detailed state-to-state air kinetics using a GPU cluster, Comput. Phys. Commun. **219**, 178 (2017).
[52] F. Esposito, I. Armenise, and M. Capitelli, N-N_2 state to state vibrational-relaxation and dissociation rates based on quasiclassical calculations, Chem. Phys. **331**, 1 (2006).
[53] F. Esposito and M. Capitelli, The relaxation of vibrationally excited O_2 molecules by atomic oxygen, Chem. Phys. Lett. **443**, 222 (2007).
[54] F. Esposito and M. Capitelli, Quasiclassical trajectory calculations of vibrationally specific dissociation cross-sections and rate constants for the reaction $O + O_2(v) \rightarrow 3O$, Chem. Phys. Lett. **364**, 180 (2002).

[55] G. D. Billing and E. R. Fisher, VV and VT rate coefficients in N_2 by a quantum-classical mode, Chem. Phys. **43**, 395 (1979).
[56] C. Coletti and G. D. Billing, Vibrational energy transfer in molecular oxygen collisions, Chem. Phys. Lett. **356**, 14 (2002).
[57] L. Cutrone, M. Tuttafesta, M. Capitelli, A. Schettino, G. Pascazio, and G. Colonna, 3d nozzle flow simulations including state-to-state kinetics calculation, in *Proceedings of the XXIX International Symposium on Rarefied Gas Dynamics*, edited by J. Fan, AIP Conf. Proc. No. 1628 (AIP, New York, 2014).
[58] D. Giordano, V. Bellucci, G. Colonna, M. Capitelli, I. Armenise, and C. Bruno, Vibrationally relaxing flow of N past an infinite cylinder, J. Thermophys. Heat Transfer **11**, 27 (1997).
[59] H. Guo, X.-N. Zhang, J. Chen, H.-P. Li, and K. Ostrikov, Non-equilibrium synergistic effects in atmospheric pressure plasmas, Sci. Rep. **8**, 4783 (2018).
[60] D. Novko, M. Alducin, and J. I. Juaristi, EleCtron-Mediated Phonon-Phonon Coupling Drives the Vibrational Relaxation of Co on Cu(100), Phys. Rev. Lett. **120**, 156804 (2018).
[61] G. Colonna, L. D. Pietanza, and M. Capitelli, Recombination-assisted nitrogen dissociation rates under nonequilibrium conditions, J. Thermophys. Heat Transfer **22**, 399 (2008).
[62] A. Guy, A. Bourdon, and M.-Y. Perrin, Consistent multi-internal-temperatures models for nonequilibrium nozzle flows, Chem. Phys. **420**, 15 (2013).
[63] T. E. Magin, M. Panesi, A. Bourdon, R. L. Jaffe, and D. W. Schwenke, Coarse-grain model for internal energy excitation and dissociation of molecular nitrogen, Chem. Phys. **398**, 90 (2012).
[64] R. N. Gupta, J. M. Yos, R. A. Thompson, and K.-P. Lee, *A Review of Reaction Rates and Thermodynamic and Transport Properties for an 11-Species Air Model for Chemical and Thermal Nonequilibrium Calculations to 30,000 K*, Reference Publication 1232 (NASA, Washington, DC, 1990).
[65] G. S. R. Sarma, Physico-chemical modeling in hypersonic flow simulation, Progr. Aerospace Sci. **36**, 281 (2000).
[66] R. B. Bird, W. E. Stewart, and E. N. Lightfoot, *Transport Phenomena*, 2nd ed. (Wiley, New York, 2002).
[67] E. A. Mason and S. C. Saxena, Approximate formula for the thermal conductivity of gas mixtures, Phys. Fluids **1**, 361 (1958).
[68] M. Capitelli, G. Colonna, and A. D'Angola, *Fundamental Aspects of Plasma Chemical Physics: Thermodynamics*, 1st ed., Springer Series on Atomic, Optical, and Plasma Physics Vol. 66 (Springer, New York, 2012).
[69] G. Colonna, M. Tuttafesta, M. Capitelli, and D. Giordano, Non-Arrhenius NO formation rate in one-dimensional nozzle airflow, J. Thermophys. Heat Transfer **13**, 372 (1999).
[70] F. Esposito, I. Armenise, G. Capitta, and M. Capitelli, O-O_2 state to state vibrational-relaxation and dissociation rates based on quasiclassical calculations, Chem. Phys. **351**, 91 (2008).
[71] F. Bonelli, A. Viggiano, and V. Magi, A numerical analysis of hydrogen underexpanded jets, in *Proceedings of the ASME 2012 Internal Combustion Engine Division Spring Technical Conference, Torino, Piemonte, Italy, May 6–9, 2012*, ICES2012-81068 (ASME Publishing, New York, 2012), pp. 681–690.
[72] J. L. Steger and R. F. Warming, Flux vector splitting of the inviscid gasdynamic equations with application to finite-difference methods, J. Comput. Phys. **40**, 263 (1981).
[73] J. G. Verwer, Gauss-Seidel iteration for stiff ODES from chemical kinetics, SIAM J. Sci. Comput. **15**, 1243 (1994).
[74] S. Nonaka, H. Mizuno, K. Takayama, and C. Park, Measurement of shock standoff distance for sphere in ballistic range, J. Thermophys. Heat Transfer **14**, 225 (2000).
[75] M. Furudate, S. Nonaka, and K. Sawada, Behavior of two-temperature model in intermediate hypersonic regime, J. Thermophys. Heat Transfer **13**, 424 (1999).
[76] C.-Y. Wen and H. G. Hornung, Non-equilibrium dissociating flow over spheres, J. Fluid Mech. **299**, 389 (1995).
[77] N. Belouaggadia, H. Olivier, and R. Brun, Numerical and theoretical study of the shock stand-off distance in non-equilibrium flows, J. Fluid Mech. **607**, 167 (2008).
[78] E. Josyula and W. F. Bailey, Vibration-dissociation coupling using master equations in nonequilibrium hypersonic blunt-body flow, J. Thermophys. Heat Transfer **15**, 157 (2001).

[79] G. Colonna, I. Armenise, D. Bruno, and M. Capitelli, Reduction of state-to-state kinetics to macroscopic models in hypersonic flows, J. Thermophys. Heat Transfer **20**, 477 (2006).
[80] G. D. Billing and R. E. Kolesnik, Vibrational relaxation of oxygen. State to state rate constants, Chem. Phys. Lett. **200**, 382 (1992).
[81] G. D. Billing, *Nonequilibrium Vibrational Kinetics* (Springer-Verlag, Berlin, 1986), Chap. 4.
[82] M. Capitelli, C. Gorse, and G. D. Billing, V-V pumping up in non-equilibrium nitrogen: Effects on the dissociation rate, Chem. Phys. **52**, 299 (1980).
[83] D. Bose and G. V. Candler, Thermal rate constants of the $N_2 + O \rightarrow NO + N$ reaction using *ab initio* $^3A''$ and $^3A'$ potential energy surfaces, J. Chem. Phys. **104**, 2825 (1996).
[84] D. Bose and G. V. Candler, Thermal rate constants of the $O_2 + N \rightarrow NO + O$ reaction based on the $A^{2\prime}$ and $A^{4\prime}$ potential-energy surfaces, J. Chem. Phys. **107**, 6136 (1997).
[85] C. Park, Review of chemical-kinetic problems of future NASA missions, I: Earth entries, J. Thermophys. Heat Transfer **7**, 385 (1993).
[86] R. C. Millikan and D. R. White, Systematics of vibrational relaxation, J. Chem. Phys. **39**, 3209 (1963).